Modeling VRALA, the next-generation actuator for high-density, tick secondary mirrors for astronomy

C. Del Vecchio*,[1], G. Agapito[1], G. Tomassi[2], and E. de Santis[2]
[1]INAF-OAA, [2]University of Cassino – DAEMI
*L. Enrico Fermi 5 I-50125 Firenze, cdelvecchio@arcetri.astro.it

Abstract: The next-generation Extremely Large Telescopes adaptive optics systems require high-order, long-stroke, quite large deformable mirrors. Higher forces and greater actuator densities than the ones provided by the current technology are needed, still maintaining the severe accuracy and bandwidth requests. Based on a very simple magnetic circuit, providing a compact device, VRALA (Variable Reluctance Adaptive mirror Linear Actuator) accomplishes this very demanding goal. With an efficiency of about 7 N/W and an overall radius that allows actuator separations as low as 25 mm, the deformable mirror can be actuated with large forces on small spatial scales, with a little thermal impact, and/or its thickness can be increased, in order to simplify the manufacturing. This paper is aimed at presenting a preliminary study of VRALA. After showing the rationale of the adopted geometrical simplifications, we discuss the numerical optimization process, as well as its analytical verification, focused to define the best performing geometry of the magnetic circuit, whose excellent static performances allows to greatly reduce the thermal impact. Adding to the magnetostatic FEM the ALE application mode and few ODEs allows to accurately investigate the open-loop dynamics of the system. Coupling Comsol with Matlab, the device is placed in a closed-loop control system, whose design is also presented, with promising results - the settling time doesn't exceed 1 ms. Two prototypes have been tested, and the first set of the measured data matches the results of the magnetostatics numerical simulations.

Keywords: ELT, Adaptive Optics, Electromagnetism, Actuator, FEA

1 Introduction

The actuators developed for the Adaptive Optics (AO) of the 8 m-class telescopes, described in [2], are not suitable for the Extremely Large Telescopes (ELT), whose optical design requires a low-order, large-thickness and long-stroke adaptive mirror. Therefore, a different design was proposed in [1], allowing to decrease by one order of magnitude the power dissipated to actuate the correction force. Nevertheless, those very good performances were obtained with a significant mechanical complexity. VRALA, whose preliminary design is outlined in this paper, with a simpler geometry an even better performances, is the ideal candidate for the ELT AO actuators. A cylindrical, hollow shaped soft iron stator accommodates a coil. The flux lines of the magnetic field produced by the current flowing in the coil are conveyed into a mover, a disk also built of soft iron and facing the stator, through an air gap. As the magnetic pressure in that gap works as a pull-only force on the mover, a second stator, placed symmetrically with respect to the mover, is needed to produce the push force. The force is applied to the deformable mirror (DM) by a shaft fixed to the mover, mounted in the stator central hole parallelly to its axis. This paper discusses the design study of VRALA, schematized in figure 1, based on a Comsol/Matlab numerical process, aimed to minimize the power needed to deliver the actuation force within the requirement listed in table 1. The optimization methods and the analytical and experimental validations of the numerical approaches are shown section 2. The dynamics of the model, in terms of open- and closed-loop responses, are discussed in section 3.

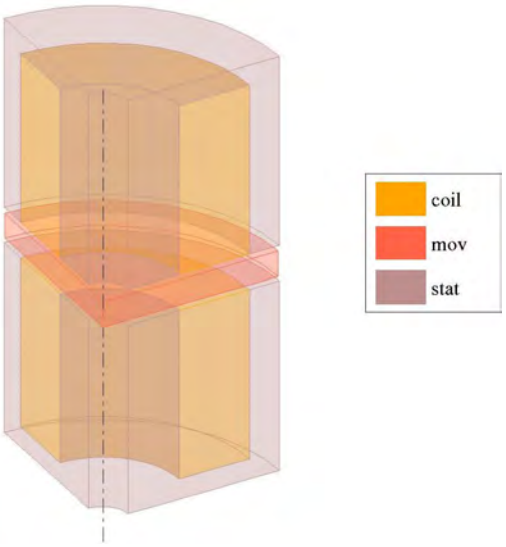

Figure 1: Schematic view of the actuator.

rms force (turbulence correction)	.363 N
max force (static)	.36 N
max force (dynamic)	1.27 N
stroke (usable)	±100 µm
stroke (mechanical)	±150 µm
bandwidth	1 kHz
typical inter-actuator spacing	25 mm
typical actuator length	≤ 60 mm
typical mover mass	≤ 10 g
DC resistance	2 to 2.5 Ω

Table 1: Basic requirement of the actuator for the high order DM.

2 Magnetostatics

2.1 Full and actual coil

Besides the modeling simplification allowed by the axial symmetry of the actuator, a further, dramatic reduction of the degrees of freedom can be obtained by replacing the coil cross section with a full rectangle in the r-z plane with the same resistivity ρ of the actual coil material, provided that the "full" coil exhibits the same response of the actual coil. Such an equivalence must be implemented in terms of both power and induced voltage when simulating the transient response. According to the definitions of figure 2 and table 2, we recall the relationships demonstrated in [3] between the actual values of the resistance R, the current density J, the magnetic force F and the voltage V and their correspondent full values, identified by the subscript f:

$$R_f = \frac{\varphi}{N^2} R \tag{1}$$

$$J_f^2 = \varphi J^2 = \varphi \left(\frac{I}{A_w} \right)^2 \tag{2}$$

$$F_f = \frac{1}{\varphi} F \tag{3}$$

$$\overline{V}_f = \frac{\sqrt{\varphi}}{N} V \tag{4}$$

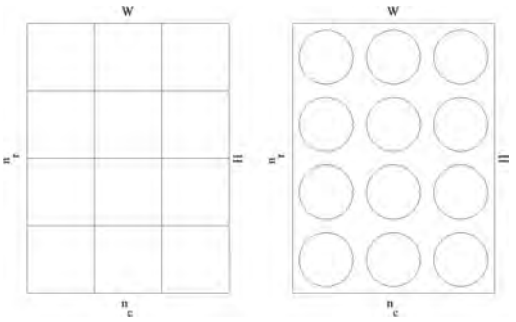

Figure 2: The coil and its full approximation.

r_w	wire radius
W	slot width
H	slot height
$\overline{R}$	slot mean radius
ρ	wire resistivity
n_c	# of turns along r
n_r	# of turns along z
$N = n_c n_r$	total # of turns

Table 2: Definitions of the coil parameters.

As demonstrated in [3], in transient, step-by-step time analyses, i.e when $\frac{d\Phi}{dt} \neq 0$, the equivalence $\overline{V}_f = V$ is satisfied if

$$J_f = N \frac{I}{A_w} \tag{5}$$

and

$$\overline{V}_{ind_f} = N \overline{V}_{ind} \tag{6}$$

2.2 Analytical optimization

Redefining r_{stat_i}, $\overline{R}-W/2$, $\overline{R}+W/2$, r_{stat_o}, and H in table 3 as R_1, R_2, R_3, R_4, and h, respectively, the optimization process discussed in [3] shows that the efficiency ϵ can be defined as

$$\epsilon = K\frac{(R_4^2 - R_3^2 + R_2^2 - R_1^2)(R_3 - R_2)}{R_3 + R_2} \quad (7)$$

where K, whose terms are defined in [3], is equal to $\frac{1}{8}\frac{\mu_0\varphi h}{\rho g^2}$. Let us set the constant dimensions according to the following constraints: $R_1 = 1.5\,\mathrm{mm}$, $R_4 = 10\,\mathrm{mm}$, $h = 12\,\mathrm{mm}$, $g = 0.2\,\mathrm{mm}$, $\varphi = 0.3$. Figure 3 shows the efficiency defined in equation 7 as a function of the variables R_2 and R_3. With the aforementioned constraints, the maximum efficiency is equal to $28.3\,\mathrm{N}\times\mathrm{W}^{-1}$.

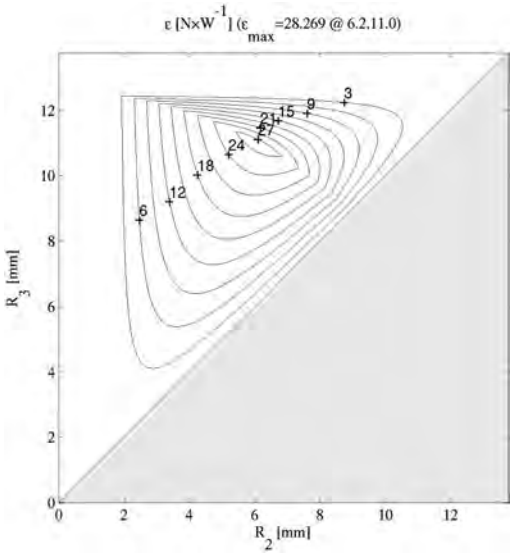

Figure 3: The efficiency as a function of R_2 and R_3. See the text for a discussion.

2.3 Numerical optimization

A single Matlab script allows to fully calculate the magnetic response of the actuator by means of a Finite Element Model (FEM), whose purpose is the evaluation of the effect of the material choices and the geometry variations on the solutions. The script, which gives results truthful and small time-consuming, provided that the mesh is both accurate and numerically smooth, can be summarized as follows:

geometry the simple basic components of the full coil geometry shown in figure 1 are built in the r-z plane defined in 2.1

meshing typically, 10000 elements are obtained and embedded in the *azimuthal currents* application mode

physics the physical properties of the chosen materials, including the air, are defined via tables or plots provided by the manufacturers; the input external current density is defined as in equation 2 and the resulting magnetic force is scaled according to equation 3

solution the non linear system — of typically 20000 equations — is solved for the magnetic potential variable A_ϕ, where ϕ is perpendicular to the r-z plane defined in 2.1

post-processing the magnetic force is computed via the Maxwell stress tensor

2.3.1 Material

Adding the Ferrite of class "R" manufactured by Magnetics® and the "Somaloy 1000", a SMC (Soft Magnetic Composite) produced by Höganäs® to the 15 soft iron materials discussed in [4] and [1] and running 17×17 models in order to investigate the response of all the possible stator/mover material combinations, shows that the 64% of the all the cases allows to obtain $\epsilon \geq 6\,\mathrm{N}\times\mathrm{W}^{-1}$. In fact, the considered soft iron materials, mostly of good magnetic properties, rarely reach the saturation zone of the B-H curve.

2.3.2 Geometry

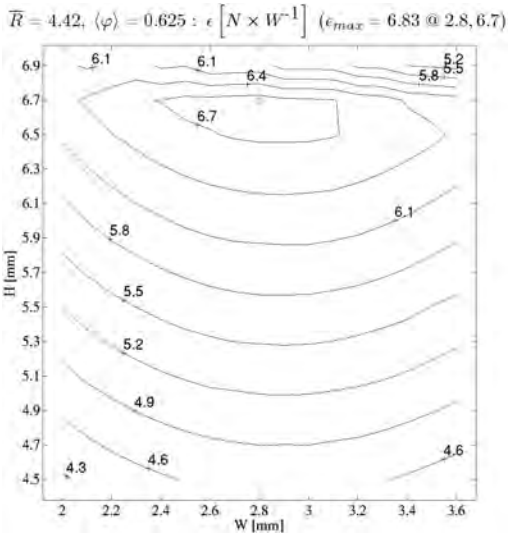

Figure 4: The efficiency as a function of W and H (see the text for a discussion).

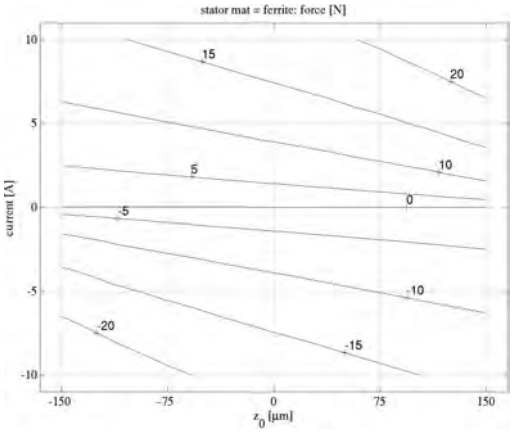

Figure 5: Force vs current and position (see text for a discussion).

Similarly to previously proposed actuators (see [2], [4], and [1]), a geometrical optimization is aimed to identity the geometry that maximizes ϵ, while fulfilling the constraints listed in table 1 — such geometrical parameters are listed in table 3. As some preliminary runs show that ϵ does not depend on h_{mov}, this value is chosen equal to 1 mm, in order to minimize the mass. Moreover, the efficiency always takes a maximum when $H = h_{slot}$ and when r_{stat_o} is equal to 7 mm — the maximum value allowed by the inter-actuator spacing limit given by the specifications. Finally, h_{stat} has been selected equal to 7.5 mm, a reasonable figure in order to satisfy the height limit of the entire assembly. Therefore, the optimization process becomes simpler — the minimum of $\epsilon = \epsilon\left(W, H, \overline{R}\right)$ is to be found. Running $\epsilon = \epsilon\left(W, H\right)$ for several values of $\overline{R}$ in the range 4.5 to 6.9 mm allows to determine that the maximum ϵ, $6.83\,\mathrm{N} \times \mathrm{W}^{-1}$, is reached when $W = 2.8\,\mathrm{mm}$, $H = 6.7\,\mathrm{mm}$, and $\overline{R} = 4.42\,\mathrm{mm}$. Figure 4 shows $\epsilon = \epsilon\left(W, H\right)$ for $\overline{R} = 4.42\,\mathrm{mm}$. This results if obtained with $r_w = 120\,\mu\mathrm{m}$, with $\tau_{ins} = 10\,\mu\mathrm{m}$, in order to match the required DC resistance, and selecting the Ferrite mentioned in section 2.3 and the Euronorm FeV 270 50H or M15 (USA AISI 1978) (see [4]) as stator and rotor materials, respectively. We note that the analytical optimization discussed in section 2.2 leads to the same conclusion — a value of $\overline{R}$ that maximizes ε can be identified.

Running the magnetostatics of the best performing geometry defined above for currents spanning from -10 to $10\,\mathrm{A}$ and mover starting positions z_0 spanning from -150 to $150\,\mu\mathrm{m}$ give the results shown in figure 5, where the negative values of the current correspond to a current flowing in the bottom coil instead of the top coil.

The full coil method has been verified firstly by running the best performing geometry with a FEM reproducing the actual coil, and secondly by running the geometry discussed in section 2.2 with the same electromagnetic approximations. The efficiency computed with Comsol, $28.19\,\mathrm{N} \times \mathrm{W}^{-1}$, is only .28% lower than the analytically computed value, shown in figure 3. Although such a value is almost three times larger than the measured value reported in table 4, the agreement with the numerical results is reached. In fact, running the FEM with $\mu_r = 200$ instead of 20000, a non realistic value, selected in order to fulfill the analytical assumptions, we obtain $\epsilon = 10.47\,\mathrm{N} \times \mathrm{W}^{-1}$, a figure very close to the measured value.

Symbol	Value [mm]	Description
r_w	.12	wire radius
τ_{ins}	.01	insulation thickness
r_{stat_o}	7	outer radius of stator
r_{stat_i}	1	inner radius of stator
h_{stat}	7.5	height of stator
h_{slot}	4.5 to 6.9	height of stator slot
g	.2	gap height
r_{mov_o}	6.95	outer radius of mover
r_{mov_i}	0	inner radius of mover
h_{mov}	1	height of mover
H	h_{slot}	height of coil slot
W	2 to 3.6	width of coil slot
$\overline{R}$	3.82 to 4.98	mean radius of coil slot

Table 3: Definitions of the geometrical parameters of optimization (see text for a discussion; use figure 1 as a reference).

2.3.3 Iron losses

Some frequency analyses, performed combining three types of iron materials — Ferrite, SMC and silicon iron, whose typical resistivities are 1, 7×10^{-7} and $5\times10^{-7}\,\Omega\times\mathrm{m}$, respectively — for the stator and the mover, have been run. Even in the worst case, i.e. when the stators and the mover are built of silicon iron, at 10 kHz the maximum resistive heating in the iron is $\leq 1.6\%$ of the DC power — such a ratio becomes negligible for all the other material combinations. Recalling the discussion about the hysteresis losses reported in [1], we can conclude that the total heating in the iron components is very low.

2.4 Prototyping

Two very simple prototypes, built of Ferrite P22/13-3C90 by Ferroxcube and of C40 (EN 10250-2:1999) steel, shown in figure 6, have been set up in order to validate both the analytical and the numerical computations, discussed in sections 2.2 and 2.3, respectively. Supplying a decreasing current to a coil of a certain resistance with a current generator, starting with a value able to keep a soft iron disk in contact with a single stator vertically placed, and measuring the current at the disengagement of the disk, gives the values of the magnetic force. The physical parameters of the above mentioned prototypes are shown in table 4, along with their efficiencies, 9.75 and $1.18\,\mathrm{N}\times\mathrm{W}^{-1}$ for the C40 and the Ferrite, respectively.

value	unit	Pure Fe	Ferrite
R_1	mm	1.5	1.5
R_2	mm	6	4.5
R_3	mm	11	9
R_4	mm	12.5	10.75
h	mm	12	5
turns	N/A	400	85
force	N	1.95	0.71
voltage	V	1	0.75
current	A	0.2	0.8
power	W	0.2	0.6
ϵ	$N\times W^{-1}$	9.75	1.18

Table 4: The physical parameters of the prototypes and the measured efficiencies.

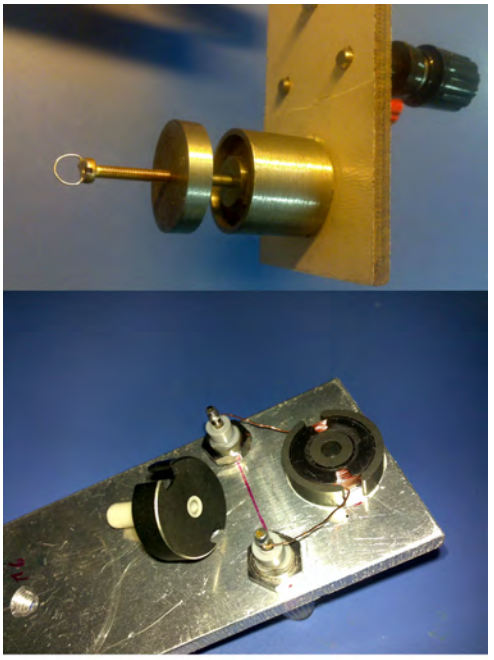

Figure 6: The C40 (top) and Ferrite (bottom) prototypes.

3 Magnetodynamics

3.1 Open loop response

3.1.1 The deformable mesh FEM

The dynamics of the system is computed as follows. Let z be the mover position, with $z = 0$ corresponding to the centered (rest) position: a dynamical FEM simulation is carried out via the *ALE* application mode, which implements a deformable mesh. Then the Ordinary Differential Equation (ODE) $F = (M + m_0)\ddot{z}$, where $M = 1.2\,\mathrm{g}$ is the mover mass and $m_0 = 10\,\mathrm{g}$ is the typical payload due to the mirror, is introduced to fully describe the dynamics of the mover. A further degree of freedom, the output current, is defined as $(V_{ext} - V_{ind})/R$, where $V_{ext} = R\,I_{ext}$ is the input applied voltage — the driving current I_{ext} is supplied according to equation 2. Finally, the induction generated in the transient is taken into account by adding to the full coil subdomain of the FEM the voltage expressed as $\overline{V}_f = \int_A \frac{(-e_f + J_f\rho)2\pi r}{A}\,dA$, whose terms are defined in [3], where J_f and

$\overline{V}_{ind_f} = \int_A \frac{e_f 2\pi r}{A} dA$ are defined by equations 5 and 6, respectively.

3.1.2 The open loop results

As any magnetic circuit has the capability to store magnetic energy, the electric variables show a non negligible time constant. This effect is quantified in figure 7, that shows the results of applying a constant I_{ext} to the FEM described in section 3.1.1 in terms of energy balance. At any time t, the input power $P(t) = Vi(t)$ is equal to the the sum of the resistive heating (both in the copper and in the iron), the kinetic power and the magnetic power. The resistive heating, mostly due to the copper losses, is minimized by the above described optimization; the magnetic power largely compensates the input power up to $\approx .8$ ms, and then is restored as kinetic power. The resulting time delay, related with the circuit impedance, along with the non linearity of the system, are the main issues that the control system approach described in section 3.2 have to address.

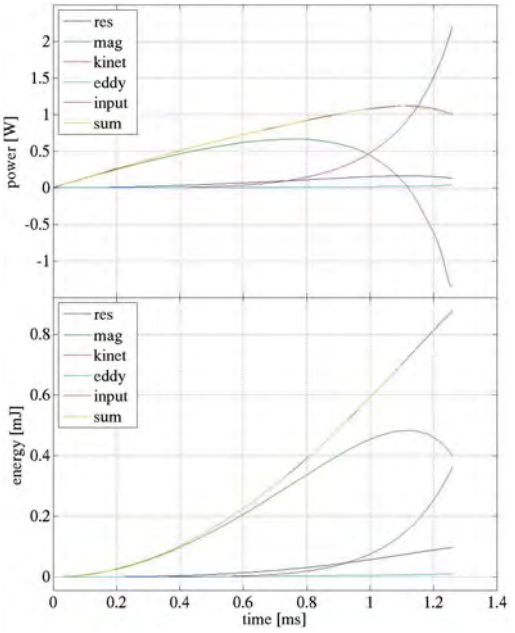

Figure 7: Open loop power (top) and energy (bottom) balance. The resistive heating in the copper is labeled as *res* and in the iron as *eddy*. The magnetic and kinetic powers and energies are labeled as *mag* and *kinet*, respectively.

3.2 Closed loop response

3.2.1 The real-time-updating LQR

The control system is based on a Linear Quadratic Regulator (LQR), and a state model representation with variable parameter.

The control system, schematized in figure 8, relies on the position feedback and the current signals, as both the velocity and the acceleration are taken from the position signal. Two Analog-to-Digital converters (A/D) sample the data at 50 kHz. The *system matrices update* determines the model system matrices $A(z, I)$ and $B(z, I)$ (see equation 10) at every step, and provides them to the LQR, which calculates the control matrix $F(k)$. This matrix multiplies the state vector to determine the control signal $u(k)$. The control, in order to be compliant with the current generator characteristics, applies a saturation on the control signal ($|I_i| \leq I_{max}$) and limits its maximum derivative ($|dI_i/dt| \leq dI_{max}$). The signal I_i is supplied to the *coil current splitter*, which provides the top coil with $I_i^t = I_i$ if $I_i > 0$, and the bottom coil with $I_i^b = I_i$ if $I_i < 0$. Moreover, the *coil current splitter* acts on the switched off coil in order to minimize the time needed to reduce the flowing current.

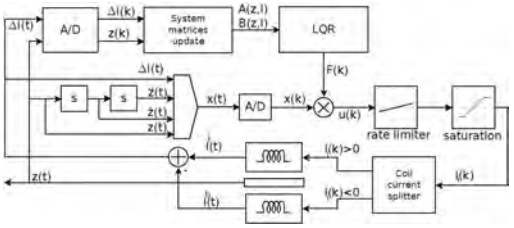

Figure 8: Closed loop scheme.

The plant can be modeled as the combination of two Transfer Functions (TF)

1. a non-linear TF between the position z, the coil current I, and the force F
2. a linear TF between input current and coil current, related with the time constant of the RL circuit

The TF 1 is a function of the position z and the coil current I: $F = f(z, I)$. F, the resultant force on the mover, is obtained from figure 5. It can be linearized at the point $p = (\bar{z}, \bar{I})$:

$$f(z, I) \approx k(p) + k_z(p)\delta z + k_I(p)\delta I \qquad (8)$$

where $k(p) = f(p)$, $k_z(p) = \left.\frac{\partial f(z,I)}{\partial z}\right|_{(p)}$ and $k_I(p) = \left.\frac{\partial f(z,I)}{\partial I}\right|_{(p)}$. The TF 2 can be modeled as a first order low-pass filter:

$$\frac{I(s)}{I_i(s)} = \frac{1}{\omega s + 1}\,, \tag{9}$$

where ω is the time constant, $I(s)$ and $I_i(s)$ are, respectively, the Laplace transforms of the coil and input current. A discrete time state space representation, with a state $x(k) = [\, I(k)\, \ddot{z}(k)\, \dot{z}(k)\, z(k)\,]'$, where the prime denotes the matrix transposition, can be obtained from equation 8 and equation 9 by a discrete time conversion:

$$x(k+1) = \mathbf{A}(p)x(k) + \mathbf{B}(p)u(k) \tag{10}$$

where $\mathbf{A}(p)$ and $\mathbf{B}(p)$ are defined as

$$\mathbf{A}(p) = \begin{bmatrix} e^{-\omega T} & 0 & 0 & 0 \\ 1 & 1 & \frac{k_z(p(k))}{m} T & 0 \\ 0 & T & 1 & 0 \\ 0 & 0 & T & 1 \end{bmatrix} \tag{11}$$

and

$$\mathbf{B}(p) = \begin{bmatrix} (1 - e^{-\omega T}) \frac{k_I(p(k))}{m} T \\ 0 \\ 0 \\ 0 \end{bmatrix} \tag{12}$$

respectively, $m = m_0 + M$ is the total mass defined in section 3.1.1, $u(k) = I_i(k)$, k is the sampled time ($t = kT$, where T is the integration time).

Assuming that the plant state at time $t = 0$ is $x(0)$, we have to find a control sequence over the regulation horizon $[0, T)$,

$$u_{[0,T)} := \{u(k)\}_{k=0}^{T-1} \tag{13}$$

which minimizes the quadratic performance index

$$J(0, x(0), u_{[0,T]}) := \|x(T)\|_Q^2 + \sum_{k=0}^{T-1} \left[\|x(k)\|_Q^2 + \|u(k)\|_R^2\right] \tag{14}$$

where $\|x\|_Q^2 := x'Qx$, and Q and R are symmetric matrices. The solution to the LQR problem (see [7]), in steady-state, is given by the following state-feedback control law:

$$u(k) = F(k)x(k)\,, \qquad k \in [0, T) \tag{15}$$

where $F = F(k)$ is the LQR feedback-gain matrix

$$F^+ = -\frac{B'PA}{R + B'PB} \tag{16}$$

and $P = P(k)$ is the symmetric non-negative definite matrix given by the solution of the following Riccati forward difference equation:

$$P^+ = [A + BF^+]' P \times [A + BF^+] + F'^+ R F^+ + Q \tag{17}$$

where F^+ and P^+ denote the $F(k+1)$ and $P(k+1)$, respectively. Note that equations 16 and 17 need to be initialized at $k_0 = 0$ by the two initial matrices F_0 and P_0. The model in equation 10 depends on the point p, hence there is a different solution for each point p. Equations 16 and 17 are modified by introducing $A = A(p)$ and $B = B(p)$ in order to consider the non linearity of the system. Moreover, in closing spirit to Recursive Least-Squares (RLS) described in [6], a forgetting factor $\lambda < 1$ is introduced in order to reduce the influence of the data belonging to the history — namely, the mover past track $\{p(j)\}_{j=0}^{k} = \{z(j), I(j)\}_{j=0}^{k}$. Thus, equations 16 and 17 become, respectively:

$$F^+ = -\frac{\lambda^{-1} B'(p) P A(p)}{R + \lambda^{-1} B'(p) P B(p)} \tag{18}$$

and

$$P^+ = \lambda^{-1} [A(p) + B(p)F^+]' P \times [A(p) + B(p)F^+] + F'^+ R F^+ + Q \tag{19}$$

3.2.2 The step response

As the step response is the most important evaluation parameter of any AO control system, we have identified with a trial-and-error approach the set of parameters able to obtain a settling time (defined as the time required for the response to rise from z_0 to $\pm 10\%$ of $z_0 + \delta$) $\leq 1\,\text{ms}$ — such parameters are summarized in table 5. The step response when commanding $\delta = 1$ to $5\,\mu\text{m}$, where $\delta = z - z_0$ is the requested stroke, is shown figure 9 for $z_0 = 0$: although the settling time for $\delta = 4$ and $5\,\mu\text{m}$ exceed by 10% the goal, the results for $\delta \leq 3\,\mu\text{m}$ are entirely within the specifications. Running the response for z_0 ranging from from -100 to $100\,\mu\text{m}$, for $\delta = 1$ and $2\,\mu\text{m}$ (figure 10), also gives good results: the settling time is

always $\leq 1\,\mathrm{ms}$. Because the maximum average power, computed over the entire time domain in figures 9 and 10, ranges from 1.3 to 10.7 mW, the thermal impact is quite low in the adaptive operations.

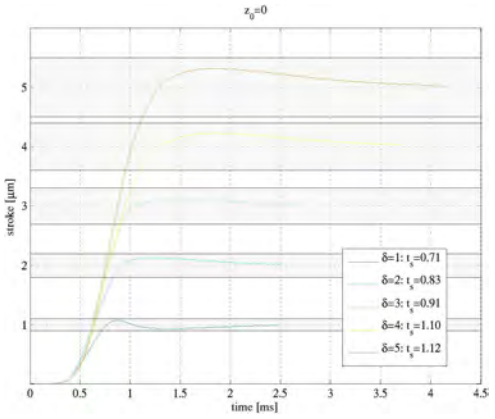

Figure 9: Step response when $z_0 = 0$. The shaded strips indicate the areas where $|(z - \delta)/\delta| \leq 10\%$.

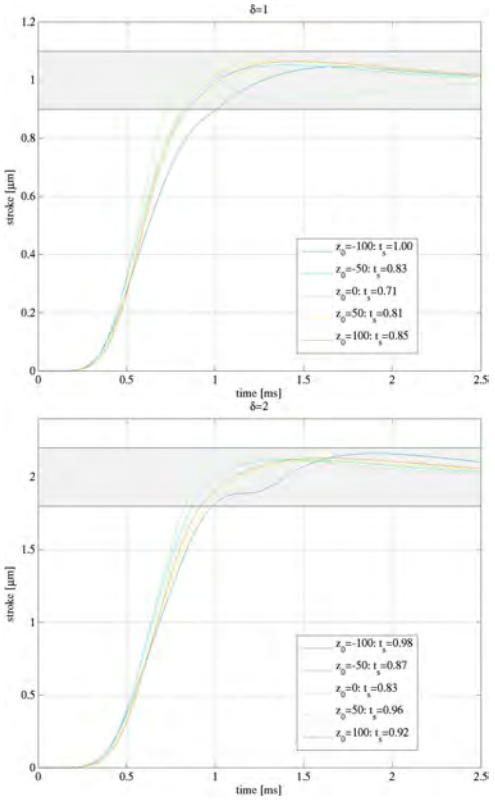

Figure 10: Step response for $\delta = 1\,\mu\mathrm{m}$ (top) and $\delta = 2\,\mu\mathrm{m}$ (bottom) with various z_0. The shaded strip indicates the area where $|(z - \delta)/\delta| \leq 10\%$.

name	value
ω cut-off frequency (see equation 9)	$3.5 \times 10^4\,\mathrm{s}^{-1}$
T sampling time (see equation 10)	$2 \times 10^{-5}\,\mathrm{s}$
L rate limiter (see Fig. 8)	$6000k^*\,\mathrm{A} \times \mathrm{s}^{-1}$ if $\delta \leq 3\,\mu\mathrm{m}$ $5000k^*\,\mathrm{A} \times \mathrm{s}^{-1}$ if $\delta > 3\,\mu\mathrm{m}$
k^* suitable constant (see L definition)	.48 to 1.35
λ forgetting factor (see equation 18)	.83 to .94
Q (see equation 14)	identity matrix of suitable dimensions
$10 \times R$ (see equation 14)	identity matrix of suitable dimensions

Table 5: Closed loop plant parameters. k^*, determined on trial-and-error basis, is used when $z_0 \neq 0$ in order to compensate the non linear relationship between the magnetic force and the displacement. λ is determined on trial-and-error basis as a function of $|\delta - z|$.

4 Future work

VRALA, the last chapter of the short but rich history of the AO technology, depicted in [5], has established many achievements. The above mentioned encouraging results indicate the near future developments. A much more realistic prototype, provided with the capacitive sensor fit for the actuator studied in [1], has to be built, in order to explore the possible construction issues, to measure the real closed loop response, and the power dissipation. In the meantime, several computational efforts will be needed: possible alternative control system techniques must be studied, the closed loop frequency response have to be computed, a multiphysics computational frame must be implemented in order to evaluate the heat transfer and the effects of the temperature changes on the magneto-mechanics of the actuator. 3D models must be developed in order to simulate the response of the system, in terms of mechanical and thermal deforma-

tions, and especially the performance variations caused by tolerances and mutual effect by close actuators. The final goal is to develop a 3D model which accommodates an array of actuators along with a portion of mirror.

5 Conclusions

The simple and very effective magnetic circuit of VRALA makes the device extremely suited for the ELT adaptive optics systems. The high-order, long-stroke, very large deformable mirrors of the next generation telescopes require very large forces and unprecedented actuator densities. The results obtained with the numerical tools developed with Comsol for VRALA, verified by two very simple, preliminary prototypes and some analytical studies, demonstrate that this actuator can accomplish those demanding specifications with a very low power dissipation and a sufficient bandwidth. With a typical efficiency of $7\,\mathrm{N} \times \mathrm{W}^{-1}$, that greatly reduces the thermal impact, and an overall radius that allows to reach an actuator separation as small as 25 mm, VRALA can provide a 1 µm stroke in .71 ms.

References

[1] Ciro Del Vecchio, Roberto Biasi, Daniele Gallieni, Armando Riccardi, and Roberto Spairani, *Actuating the deformable mirror: a multiphysics design approach*, Advanced Optical and Mechanical Technologies in Telescopes and Instrumentation (Eli Atad-Ettedgui and Dietrich Lemke, eds.), Proc. SPIE, vol. 7018, SPIE, 6 2008, pp. E.1–E.11.

[2] Ciro Del Vecchio, Daniele Gallieni, Hubert M. Martin, Armando Riccardi, Guido Brusa, and Roberto Biasi, *Design improvements of the LBT adaptive secondary*, Beyond Conventional Adaptive Optics (Elise Vernet, Roberto Ragazzoni, Simone Esposito, and Norbert Hubin, eds.), Proc. ESO, vol. 58, ESO, 5 2001, pp. 435–441.

[3] Ciro Del Vecchio, Fabrizio Marignetti, Guido Agapito, Giovanni Tomassi, and Armando Riccardi, *Vrala: Designing and prototyping a novel, high-efficiency actuator for large adaptive mirrors*, Adaptive Optics Systems (Brent L. Ellerbroek, Michael Hart, Norbert Hubin, and Peter L. Wizinowich, eds.), Proc. SPIE, vol. 7036, SPIE, 6 2010.

[4] Ciro Del Vecchio, Fabrizio Marignetti, Armando Riccardi, Maurizio Scarano, and Paolo Cancelliere, *Selecting the electromagnetic actuator of the ELT primary mirror*, Advances in Adaptive Optics II (Brent L. Ellerbroek and Domenico Bonaccini Calia, eds.), Proc. SPIE, vol. 6272, SPIE, 5 2006, pp. 157–167.

[5] Ciro Del Vecchio, Armando Riccardi, Fabrizio Marignetti, Roberto Biasi, Daniele Gallieni, and Roberto Spairani, *Linear motors for astronomical mirrors*, Industry Applications Society Annual Meeting, 2008. IAS '08. IEEE, 10 2008, pp. 1–8.

[6] Lennart Ljung, *System identification: Theory for the user (2nd edition)*, Prentice Hall PTR, December 1998.

[7] Edoardo Mosca, *Optimal, predictive, and adaptive control*, Prentice-Hall, Inc., Upper Saddle River, NJ, USA, December 1995.

Acknowledgements

The authors would like to thank Mauro Marchesi from Ferroxcube Italy, for having provided them with the ferrite samples used to build the ferrite prototype, and Riccardo Crosa from Höganäs Italy, for insight and guidance through the Somaloy materials.